Direct Laser Writing of Volumetric Gradient Index Lenses and Waveguides

Christian R. Ocier[1,2,3,8], Corey A. Richards[1,2,3,8], Daniel A. Bacon-Brown[1,2,3], Qing Ding[4], Raman Kumar[4], Tanner J. Garcia[2,3], Jorik Van de Groep[5], Jung-Hwan Song[5], Austin J. Cyphersmith[6], Andrew Rhode[1,2,3], Andrea N. Perry[1,2,3], Alexander J. Littlefield[4], Jinlong Zhu[4], Dajie Xie[1,2,3], Haibo Gao[1,2,3], Mark L. Brongersma[5], Kimani C. Toussaint[7], Lynford L. Goddard[4*], and Paul V. Braun[1,2,3,7*]

[1]Department of Materials Science and Engineering, University of Illinois at Urbana-Champaign, Urbana, IL, USA. [2]Materials Research Laboratory, University of Illinois at Urbana-Champaign, Urbana, IL, USA. [3]Beckman Institute for Advanced Science and Technology, University of Illinois at Urbana-Champaign, Urbana, IL, USA. [4]Department of Electrical and Computer Engineering, University of Illinois at Urbana-Champaign, Urbana, IL, USA. [5]Department of Materials Science and Engineering, Stanford University, Stanford, CA, USA. [6]Carl R. Woese Institute for Genomic Biology, University of Illinois at Urbana-Champaign, Urbana, IL, USA. [7]Department of Mechanical Science and Engineering, University of Illinois at Urbana-Champaign, Urbana, IL, USA. [8]These authors contributed equally: Christian R. Ocier, Corey A. Richards. *email: lgoddard@illinois.edu, pbraun@illinois.edu

Abstract

Direct laser writing (DLW) has been shown to render 3D polymeric optical components including lenses, beam expanders, and mirrors with sub-micrometer precision. However, these printed structures are limited to the refractive index and Abbe number of the photopolymer. Here we present Subsurface Controllable Refractive Index via Beam Exposure (SCRIBE), a lithographic approach that enables tuning of refractive index over a range of greater than 0.3 and the Abbe number, by performing DLW inside photoresist-filled nanoporous silicon and silica scaffolds. Adjusting laser exposure during printing enables 3D submicron control of polymer infilling, and thus refractive index and chromatic dispersion. Combining SCRIBE's unprecedented index range and 3D writing accuracy led to the realization of the world's smallest (15 μm diameter) spherical Luneburg lens operating at visible wavelengths. SCRIBE's ability to tune chromatic dispersion alongside refractive index was leveraged to render achromatic doublets in a single printing step, eliminating the need for multiple photoresins and writing sequences. SCRIBE also has demonstrated potential for combining optical components within a volumetric integrated circuit. As a demonstration, an all-pass ring resonator was coupled to a subsurface 3D waveguide. The measured quality factor of 4,600 at 1550 nm suggests the possibility of compact photonic systems with optical interconnects that traverse multiple planes. SCRIBE is uniquely suited for constructing such photonic integrated circuits due to its ability to integrate multiple optical components including lenses and waveguides without additionally printed supports.

Introduction

Multiphoton direct laser writing (DLW) is an emerging submicron-scale additive manufacturing technique for fabricating miniaturized three-dimensional (3D) photonic devices[1–5]. In DLW, optical components are formed with submicron voxel resolution in photoresist by a pulsed femtosecond laser via a multiphoton polymerization process[6]. DLW has been used to form lenses[2,7–9], mirrors[3,10], waveguides[11], photonic crystals[4,7,12], phase masks[13,14], and other related optical elements for beam shaping, imaging, and photonic integration. While DLW is now widely accessible due to advancements in instrumentation and photoresist chemistries[1,15,16], DLW-fabricated microscale optics remain limited by the photoresist's single refractive index[17,18]. Furthermore, the DLW process precludes fabrication of free-standing elements, limiting the formation of compound lenses and intricate waveguiding photonic networks.

Here we present Subsurface Controllable Refractive Index via Beam Exposure (SCRIBE), a lithographic approach that transforms the purview of devices that can be rendered with DLW. Using SCRIBE, microscale subsurface optics including gradient and single index lenses, compound lenses, waveguides, and other optical elements are generated inside the volume of thick porous silicon (PSi) and porous silicon dioxide ($PSiO_2$) films. The mesoporous hosts suspend the 3D structures and stabilize variable filling fractions of cross-linked photoresist, enabling refractive index control over a broad range ($\Delta n > 0.3$ at visible wavelengths). Changing the laser power as the beam writes enables the fill fraction and thus the refractive index to be spatially varied with sub-micron resolution.

With SCRIBE we present the first 3D gradient index (GRIN) fabrication process that attains submicron spatial and refractive index resolution. SCRIBE lithography's parametric versatility enables geometric and GRIN configurations previously unachievable with conventional DLW.

Microlenses presented in this work include doublets chromatically corrected across visible wavelengths and 3D Luneburg lenses that feature spherical refractive index profiles and geometries. The 15-μm diameter spherical Luneburg GRIN lens illustrates one of the most powerful manufacturing advantages of SCRIBE in its ability to simultaneously control geometry and refractive index in 3D space. This Luneburg lens focuses light at visible wavelengths and is the smallest spherical Luneburg lens we are aware of to this date. Furthermore, we take the first steps towards volumetric photonic integration by printing suspended 3D single mode waveguides coupled to all-pass microring resonators. A measured loss of 2.5 dB/mm suggests SCRIBE's potential for designing densely packed optical elements across multiple planes. SCRIBE ultimately demonstrates design versatility that complements existing multiphoton lithography approaches used for optical component fabrication.

Results

Broad Continuous Microscale Refractive Index Control

SCRIBE generates subsurface optical elements by focusing a pulsed femtosecond laser to locally polymerize a negative tone photoresist inside a porous medium. The filling fraction of polymerized photoresist inside the mesoporous scaffold is modulated by controlling the laser exposure during writing, resulting in an unprecedented tunable refractive index range of 1.28 (index of unfilled scaffold) to 1.85 for 633 nm light. Figure 1a depicts how this index range can be utilized to produce a GRIN Luneburg lens that focuses visible wavelengths. This 3D spatial control of the degree of polymerization allows the fabrication of geometric, compound, and GRIN optics, as well as integrated photonics (Fig. 1b).

The geometries and cross-linking densities of printed structures are experimentally observed using multiphoton fluorescence microscopy[19]. The geometric fidelity of SCRIBE is validated by printing and imaging simple shapes inside PSi (Fig. 2a). Since fluorescence intensity is a proxy for polymer-filling fraction, the index profile of a structure can also be qualitatively determined via multiphoton microscopy. Figure 2b shows fluorescence images from three geometrically identical prisms written with successively higher average laser powers (5, 10, and 15 mW) visualized under the same imaging conditions. The prisms written at higher laser exposures exhibited relatively higher fluorescence intensities. A checkerboard structure printed with alternating average laser powers (7.5 and 15 mW) and imaged with multiphoton microscopy, shown in Supplementary Information (SI) Section 1, further demonstrates SCRIBE's volumetrically precise control of refractive index within a single object.

Shifts in refractive index are visibly demonstrated by cross-linking large-area patterns inside PSi-based distributed Bragg reflectors (DBRs). The PSi DBR's stopband is determined by the refractive indices and thicknesses of the alternating layers. The reflection peak is expectedly red shifted by >100 nm when the pores are infilled, with larger red shifts corresponding to higher index secondary materials[20,21]. In Fig. 2c, submicron regions of a blue DBR (initial stopband at 495 nm) are spectrally shifted to generate 120 μm diameter University of Illinois seals including a seal red shifted to adopt the university's orange and blue motif. As a demonstration of larger area patterning using SCRIBE, a 5 mm by 7 mm green University of Illinois block "I" was fabricated inside a blue DBR by stitching 300 μm by 300 μm exposure fields together (Fig. 2d).

Voxel Dimensions Measurements

In multiphoton polymerization, voxels formed at the focal spot of a pulsed laser are the fundamental building blocks of 3D printed objects. The voxel's shape is determined by the

asymmetric point spread function (PSF), and thus are ellipsoids that are larger in the axial (z) direction[22]. The lateral dimensions of voxels formed using DLW have been previously documented for regular substrates by printing lines and measuring their x and z dimensions[23]. However, the PSF is altered when the laser is focused inside a porous scaffold. By writing lines inside PSi and $PSiO_2$, cleaving the samples, and viewing the cross-sections, the lateral and axial dimensions of the subsurface voxels can be determined. Scanning electron micrographs of selected voxels embedded in $PSiO_2$ are shown in Fig. 3a. The voxels' x and z dimensions for different exposure powers are measured from the contrast between the native scaffold and line arrays.

Voxels written in both scaffolds show an increase in size in both the x and z dimensions with increasing laser exposure, represented by the best-fit ellipse diagrams in Fig. 3b for PSi and Fig. 3d for $PSiO_2$. The best-fit ellipses were found by measuring the dimensions of 20 voxels printed at each laser power. The trends in the scaling of the voxel size with respect to laser exposure is graphically shown in the elliptical contour plots, where the central red voxel represents the lowest exposure conditions needed for observable cross-linking, and the outer dark blue voxel represents the exposure condition before the pulsed laser ablates the photoresist. The explicit average dimensions of the voxels printed inside both materials are also graphically depicted in Fig. 3c and Fig. 3e for PSi and $PSiO_2$, respectively. With the voxel dimensions quantified with respect to laser power, 3D structures can be fabricated with precise geometries.

Refractive Index Characterization

The effective refractive index of features formed via SCRIBE as a function of laser write power was determined by writing and characterizing subsurface Fresnel biprisms inside PSi and $PSiO_2$ (Fig. 4). A Fresnel biprism refracts light, forming a periodic interference pattern at the output[24–29]

as depicted in Fig. 4a. We illuminate the embedded biprisms with a laser and measure the resulting fringe spacing in air. For this configuration, the effective refractive index of the SCRIBE-rendered biprism (n_{prism}) can be determined using

$$n_{prism} = \sqrt{n_{PSi}^2 sin^2\alpha + \frac{\left[\frac{\lambda_{laser}}{2d_{fringes}} + \frac{n_{PSi}\, sin(2\alpha)}{2}\right]^2}{sin^2\alpha}} \quad (1)$$

where $d_{fringes}$ is the output fringe spacing, λ_{laser} is the illuminating wavelength, n_{PSi} is the background refractive index of the porous host (measured by ellipsometry), and α is the prism angle, which is defined by adjusting the prism height and width. As expected, the fringe spacing decreases with increasing laser writing power.

Equation (1) assumes that the polymerized region within the porous scaffold is optically isotropic. While this approximation is valid for $PSiO_2$ scaffolds, PSi is highly birefringent. PSi etched under the conditions used for these experiments showed a birefringence of ~0.15[30], with the fast axis corresponding to the optical axis. When the PSi is infilled with polymerized photoresist, the birefringence is reduced but remains present, making it necessary to verify that the isotropic approximation in Equation (1) is valid for this scaffold. Birefringent biprisms were modeled in COMSOL Wave Optics with varying ordinary (n_o) and extraordinary (n_e) refractive indices. The simulated biprisms were illuminated as described in Fig. 4a, and $d_{fringes}$ was measured. The simulated fringe spacing consistently matches the fringe spacing calculated using Equation (1) given that the simulated n_o equals n_{prism} in the equation. The illuminating wavevector is mostly parallel to the optical axis if the refraction angle is small, so for PSi $n_{prism} = n_o$ when α is small ($\alpha \leq 50°$). Similarly, for the other optical elements in this work that are

embedded in PSi scaffolds, the bending angle is sufficiently small such that Equation (1) is valid. Further discussion on these simulations is available in SI Section 2.

Figure 4b depicts simulated and experimental fringe patterns for a prism with n_{prism} = 1.82 embedded inside PSi with n_{PSi} = 1.28. The *xz*-plane intensity profile of the biprism was recorded using a confocal microscope under 633 nm plane wave illumination. The line cut comparing the interference fringe pattern produced by the simulated and fabricated devices in Fig. 4c confirms a match between experiment and simulation.

Wavelengths of 488, 543, and 633 nm were used to capture n_{prism} for a range of average laser writing powers. Figure 4d-e shows the refractive index as a function of writing power at these wavelengths for biprisms written in PSi and $PSiO_2$. Error bars are the standard error across 10 different prisms for each wavelength and average writing power. The plotted ranges of refractive index at 633 nm accessible using SCRIBE are 1.54-1.85 and 1.36-1.58 for features written in PSi and $PSiO_2$, respectively. The bounds of the range of continuous index tuning are set by the threshold laser polymerization power at which prisms with good geometric fidelity were formed (lower bound) and the laser-induced damage limit (upper bound). The refractive index can be lower than the minimum indices plotted in Fig. 4d-e, but index measurements using these extremely low index prisms were unreliable. The data graphed in Fig. 4d-e is extrapolated when designing optical elements such as GRIN lenses that require a higher index difference than 0.3. The refractive index of the host material provides the background index for the cross-linked geometries, which at 633 nm is 1.28 (PSi) and 1.13 ($PSiO_2$).

Lenses with Chromatic Dispersion Control

Lenses made from dispersive materials exhibit chromatic aberrations, which is typically corrected for by combining lenses with different dispersions and curvatures into compound optical elements[31]. Lenses formed inside PSi are dispersive (Fig. 4d) and are therefore expected to exhibit wavelength dependent focusing. The highly dispersive regions of unfilled PSi above and below the lens act as additional lenses with complimentary dispersions and geometries. As shown here, the net result is that the chromatic focusing behavior of lenses formed via SCRIBE differs considerably from lenses printed in air. The surrounding PSi alters the chromatic aberration curve, transforming a dispersive singlet into an achromat.

Three 40 μm diameter lenses were fabricated inside PSi as visualized in Fig. 5a: a planoconvex singlet, a biconvex singlet, and a Fraunhofer doublet. The cross-sections are imaged using multiphoton microscopy, where the fluorescence intensity corresponds to the fill fraction of the polymerized photoresin. This is most evident in the doublet where a change in fluorescence intensity marks the cross-sectional outline. The design parameters of each lens are outlined in Table 1, including radius of curvature (ROC), thickness, lens material, and Abbe number of each region. The dispersive characteristics of the different printed regions account for the chromatic behavior observed for these elements.

Table 1: Parameters for the chromatically corrected lenses.

	Surface	ROC (µm)	Thickness (µm)	Material	Abbe Number
Plano-convex	1	∞	15	PSi	3.8
	2	50	10	PSi/PR (12.5 mW)	13.0
Biconvex	1	∞	12.5	PSi	3.8
	2	50	10	PSi/PR (12.5 mW)	13.0
	3	-50	2.5	PSi	3.8
Fraunhofer Doublet	1	∞	5.5	PSi	3.8
	2	50	10	PSi/PR (7.5 mW)	11.1
	3	-50	7	PSi/PR (12.5 mW)	13.0
	4	-30	2.5	PSi	3.8

The PSi surrounding each lens acts like a highly dispersive “flint glass” since its Abbe number is always lower than the polymerized regions. This effectively transforms a planoconvex lens printed inside PSi at the surface into an achromatic doublet and a biconvex lens into a triplet with even further reduction in chromatic aberrations. Figure 5b depicts the chromatic aberration curves for these two lenslets inside PSi. The curves for the planoconvex and biconvex lenses show achromatic focusing behavior, with the focal length at 488 nm matching that at 633 nm in both cases. The additional curved surface and the additional PSi region above the biconvex lens have the effect of reducing the chromatic focal shift from 5 µm for the planoconvex lens to 0.8 µm for the biconvex lens.

The varying of the Abbe number with writing power underscores SCRIBE's potential to engineer the chromatic focusing of multicomponent lenses. As a demonstration, a Fraunhofer doublet was formed inside PSi where each lens was printed at a different power. By engineering the ROCs and Abbe numbers of the two lenses, the Fraunhofer doublet was designed to reverse the sign of the concavity of its chromatic aberration curve while maintaining a small chromatic focal shift (~1.87 μm). This effect is highlighted in Fig. 5b, which shows how the element's focal length at 543 nm is shorter than at 488 and 633 nm. A focal profile comparison (Fig. 5c) shows close agreement between the measured and simulated back focal length (BFL) and numerical aperture (NA), 32 μm and 0.44 (simulation) and 31 μm and 0.43 (measurement).

Planar and 3D GRIN Lenses

GRIN lenses have long been proposed as an alternative to geometric optics due to their ability to reduce geometric aberrations[32]. A common GRIN optic is a planar lens with a radially varying the refractive index[33]. SCRIBE was used to construct such a 20 μm diameter flat axicon by radially modulating laser exposure such that the index profile follows:

$$n(r) = n_{center} - \frac{n_{center} - n_{edge}}{R_{lens}} * r \quad (2)$$

Where n_{center} and n_{edge} were set at 1.8 and 1.6 for 633 nm light, respectively. The planar axicon's index distribution is depicted in Fig. 6a and was visualized using multiphoton fluorescence microscopy (Fig. 6b), where the peak fluorescence intensity at its center corresponds to the region of highest refractive index.

This planar axicon outputs a Bessel-like beam with a ring-shaped intensity distribution (SI Section 3) when illuminated with a plane wave. The cross-section of the device's output agrees with the simulation in Fig. 6c, verifying SCRIBE's ability to accurately define refractive index in

planar optical elements. Various other flat elements that function as parabolic lenses or cubic airy beam phase masks can be generated by altering n(r) in Equation (2) (SI Section 4). As we now discuss, these same design principles can be extended to three dimensions to form spherical GRIN lenses and other volumetric elements with arbitrary geometries and index profiles.

A Luneburg lens is an aberration and coma-free lens with a spherically symmetric refractive index profile (Fig. 6d) that follows Rudolf Luneburg's solution[34]:

$$n_{Luneburg} = \sqrt{2 - \left(\frac{r}{R_{lens}}\right)^2} \tag{3}$$

A Luneburg lens is a unique GRIN element that focuses incident rays to its opposite surface in a manner unobtainable in spherical homogenous refractive index lenses. To date, the smallest Luneburg lenses were manufactured with DLW by structuring 3D metamaterials containing unit cells with gradient volumetric variations of polymer and air[35]. However, the unit cell sizes achievable with the resolution of DLW restricts the devices' operation to infrared wavelengths. Prior to this work, no fabrication technique has yielded a spherical Luneburg lens that focuses visible light.

SCRIBE's ability to spatially modulate refractive index within a 3D geometry provides the basis for a visible wavelength Luneburg lens. A 15 μm spherical Luneburg lens was realized by rastering the laser exposure volumetrically inside the element. The refractive index profile of this Luneburg lens is equivalent to Equation (2) but offset by the refractive index at the surface of the lens:

$$n_{Luneburg} = n_{surface} - n_{air} + \sqrt{2 - \left(\frac{r}{R_{lens}}\right)^2} \tag{4}$$

The GRIN profile of the lens was visualized by capturing a multiphoton fluorescence image at the spherical midsection of the printed lens (Fig. 6b), where the gradient index is represented by a gradual change in fluorescence intensity from center to edge.

Luneburg lenses were designed and characterized at different wavelengths. Figure 6c shows the cross-sections of the 15 μm spherical Luneburg lenses focusing 488 and 633 nm light to their opposite surfaces (top view in SI Section 3). As with any Luneburg lens, the NA is measured to be 0.707. The resolution-limited measured full width at half maximum (FWHM) were 0.37 and 0.41 μm at 488 and 633 nm, respectively.

3-Dimensional Waveguides and Integrated Photonics

A unique aspect of SCRIBE is its ability to define fiber-like structures across three dimensions, enabling the formation of multiplanar waveguides. A U-shaped GRIN waveguide coupled to a ring resonator was printed to demonstrate the 3D routing of light and enable quantitative measurements of the optical propagation loss. Figure 7 shows the U-shaped subsurface 3D waveguide printed in $PSiO_2$ where both ends curve upwards and terminate at the top surface. The waveguide accepts light from an input fiber above the surface, guides the light through a 90° bend and straight bus waveguide, couples it to an all-pass microring resonator lying in a plane parallel to the surface, and turns again the light 90° back up to the surface for collection by an output fiber. The 1 μm diameter single mode GRIN waveguide was designed and fabricated, considering the elliptical PSF of the writing process, as described in SI Section 5, where single index 1 μm diameter waveguides are also discussed.

Figure 7a shows a 3D multiphoton microscopy reconstruction of the integrated device, which consists of a subsurface 3D waveguide and a 60 μm diameter microring resonator with the same

cross-sectional GRIN profile as the waveguide (top view in Fig. 7b). The submicron gap between the microring resonator and the 3D bus waveguide is visible in the image. The gap was varied in 100 nm increments to determine the critical coupling condition (detailed discussion of device design is included in the methods section).

The transmission spectrum for the device with a 600 nm gap between the waveguide and ring resonator is graphed in Fig. 7c. This device is close to being critically coupled. The measured microring resonances are superimposed on top of Fabry-Perot oscillations formed by the cavity of the bus waveguide with the input and output ports acting as two facets. The inset in Fig. 7c shows the dip near 1539.5 nm from which a FWHM of 0.36 nm and Q of 4,310 is extracted. The dip near 1547.5 nm has a FWHM of 0.33 nm and Q of 4,630. Figure 7d shows transmission spectra for the 400 nm and 800 nm gaps, corresponding to over- and under-coupling, respectively. A rigorous loss analysis is included in SI Section 6, where the observed resonances are used to extract the loss coefficient α and the transmission coefficient t_d using Equation (S3). The loss for the subsurface GRIN waveguide is estimated to be 2.5 dB/mm (the loss estimate for the single index waveguides is 3.3 dB/mm, SI Section 5). It is not surprising that these values are noticeably greater than the 0.72 dB/mm and 0.23 dB/mm losses for step-index rectangular cross-section 60-μm diameter microrings made with lithium niobate and silicon nitride cores, respectively, because those systems use electron beam lithography to minimize scattering loss from sidewall roughness and leverage a slightly higher core-cladding index contrast (0.77 and 0.53, respectively, versus ~0.4 here) to maximize mode confinement and minimize bending loss[36,37]. Nevertheless, we suggest these loss and Q values are adequate for making small aerial footprint networks of waveguides for routing optical signals in 3D and filters for dense wavelength division multiplexing.

Discussion

We conclude with a discussion on the utility of the SCRIBE lithographic approach for the 3D microfabrication of optical elements. SCRIBE lithography combines the geometric fidelity of DLW with an effective medium materials platform to engineer new classes of optics with unprecedented spatial control over refractive index. SCRIBE enabled the formation of the first visible wavelength 3D Luneburg lens. SCRIBE is also capable of realizing multicomponent geometric lenses that control chromatic dispersion, and 3D waveguides that couple light across multiple dimensions. As an early exploration of another type of compound focusing element that cannot be easily fabricated with traditional DLW, we fabricated cascaded photonic nanojet generators (see SI Section 7).

We suggest GRIN lenses made using SCRIBE lithography merit consideration as wavefront shaping devices in compact imaging systems. SCRIBE achieves an index range of 0.3 or greater across visible wavelengths and can be arbitrarily modulated, enabling flat gradient index microlenses. By arranging flat microscale lenslets into densely packed arrays, applications such as spherical aberration-free light field microscopy may be realized[38]. Furthermore, cascaded multilevel lenses with different form factors can generated by SCRIBE in a manner that parallels the versatility and small footprint of metalenses. Additional applications we envision are interfacing with CMOS sensors, collimation, and diffusers for laser systems such as vertical-cavity surface-emitting lasers (VCSELs).

Single mode waveguides were demonstrated in three dimensions using SCRIBE, suggesting the possibility of vertical photonic integration. Three-dimensional waveguides have previously been demonstrated by altering the local refractive index of glass and silicon using a femtosecond pulsed laser[39,40]. While the SCRIBE-generated waveguides are lossier than these and

conventional waveguides, SCRIBE's ability to define waveguides with high index contrast and integrate a diverse set of optics makes it uniquely suitable for shortrange optical interconnects that traverse multiple planes.

In conclusion, we have demonstrated a new approach we term SCRIBE for the fabrication of optical elements by using a scaffold that supports structures containing variable photoresist fill fractions. Our approach offers submicron resolution over an unprecedented 3D refractive index range of more than 0.3, which has allowed for the fabrication of a variety of optical elements including the world's smallest Luneburg lens. We believe that this new approach will inspire an abundance of research, not only for the integration of SCRIBE into other technologies, but also the exploration of new materials systems that can improve upon some of the shortcomings of the materials used here. For example, development of new photoresists that have high resolution and low fluorescence will enable bioimaging applications. Design of high refractive index photoresists will expand the tunability of optics printed with SCRIBE. Increasing the current maximum achievable index contrast from 0.57 to 1.0 could allow for the fabrication of unique optics such as Maxwell fisheye lenses, Eaton lenses, and electromagnetic blackholes. The investigation of new scaffolding materials with transparency at different wavelengths and lower losses will broaden the potential application space.

Materials and Methods

Porous Silicon Etching

Diced silicon wafers (Prolog, boron doped, 0.001 Ω-cm resistivity, (100)-orientation double side polished, 500 μm thick) were rinsed with acetone, DI water, and isopropyl alcohol and dried with nitrogen. The silicon chips were placed in a polypropylene cell and sealed with an O-ring that exposed a circle with an area of 1.23 cm^2. The back side of the silicon was in contact with a stainless-steel electrode. The silicon was submerged in an electrolyte with a 1:1 volume ratio of ethanol and aqueous 48% hydrofluoric acid. A counter electrode made of a 5 mm diameter platinum-iridium inoculating loop was submerged in the electrolyte 2.5 cm above the silicon. An SP-200 Potentiostat delivered current to the wafer at a current density of 400 mA/cm^2, porosifying the silicon in the exposed region. The applied current density was alternated between 400 mA/cm^2 and 300 mA/cm^2 during DBR fabrication. After the silicon was porosified, the HF electrolyte was carefully removed from the cell and the silicon wafer was rinsed thoroughly with ethanol. Samples that operate in transmission were transferred to transmissive substrates such as fused silica or alumina. To accomplish this, the porous silicon was electrochemically detached from the silicon chip by electropolishing the film under a high current density (400 mA/cm^2) in an electrolyte composed of a 5:1 volume ratio of ethanol to aqueous 48 wt% hydrofluoric acid. The free-standing porous silicon membranes were then transferred onto these substrates using a gentle stream of ethanol.

Thermal Oxidation

Porous silicon was converted into porous silicon dioxide by thermal oxidation. The oxidation was carried out in a Lindberg Heavy-Duty Lancer M-300 oxidation tube with mass flow control (MFC) of the gases. The porous silicon films, prepared either as on-silicon chips or transferred

samples, were introduced into the furnace at a temperature of 400 °C in a nitrogen environment. The temperature was slowly increased and when the furnace temperature stabilized at 900 °C, the N_2 gas flow was switched off and dry O_2 gas was introduced into the furnace at a flow rate of 8 sccm. After thirty minutes of oxidation, the O_2 gas flow was terminated and N_2 gas flow was reintroduced during cooling. When the furnace reached a temperature of 500 °C, the sample was removed from the furnace to be used for SCRIBE fabrication.

SCRIBE Lithography

All subsurface structures were fabricated using a Nanoscribe Photonic Professional GT microscale 3D printer equipped with a femtosecond-pulsed (100 fs, 80 MHz, 50 mW avg, 6.25 kW peak) fiber laser (FemtoFiber Pro, Toptica Photonics) with its operating wavelength centered at 780 nm and a high numerical-aperture index-matched immersion objective (63×, NA = 1.4). Geometric micro-optic and gradient index elements were designed using Computer Aided Design software (MATLAB, AutoCAD, and SOLIDWORKS) and input into the Nanoscribe DeScribe rendering software interface. Rendering files for all optical elements were programmed to use the Nanoscribe's galvanometric scanning mechanism to define lateral features and the piezo actuator to structure the objects axially, allowing the fast, layer-by-layer construction of 3D architectures.

PSi and $PSiO_2$ were selected as the porous scaffolds due to their low absorption coefficients (SI Section 8) at the pulsed laser source's excitation wavelength. The porous films were infilled by dripping a commercially available negative-tone photoresist ((2-(hydroxymethyl)-2-[[(1-oxoallyl)oxy]methyl]-1,3-propanediyl diacrylate, known as IP-Dip) onto the porous films under vacuum. Two-photon polymerization of subsurface structures was carried out by positioning the laser focal spot within the volume of the PSi/photoresist region, and objects were formed at a

writing speed of 10 mm/s, with the galvanometric mirror acceleration set to 1 mm/s^2. The laser exposure delivered during the writing process was altered to modify the degree of polymer cross-linking inside the porous scaffold. 3D architectures that are laterally larger than the writing field of view (150 μm) are stitched by dividing the writing process between multiple unit blocks split from the originally designed structure. The samples were developed in a bath of 99.5% propylene glycol monomethyl ether acetate to remove traces of the non-polymerized resist, rinsed in isopropanol for 1 minute, and dried under nitrogen.

Ellipsometry

The optical constants of the unfilled PSi and $PSiO_2$ films were measured and extracted using a J.A. Woollam VASE ellipsometer. Variable angle spectroscopic ellipsometry (VASE) data and oblique incidence reflectance were measured between 400 to 1100 nm at incident angles of 45º, 60º, and 75º. Refractive index dispersions were extracted from ellipsometric and reflectance data using a biaxial effective medium fitting model included in the J.A. Woollam VASE analysis software.

Intensity Profile Confocal Imaging

A WITec Alpha 300 S upright confocal microscope fit with a 100x Zeiss Epiplan-Apochromat objective (NA = 0.95) was used to perform *xz*-plane optical intensity depth scans of the SCRIBE-written optical elements' focal behaviors. Free-space gas lasers were used for plane wave illumination of the samples at wavelengths of 488 nm (Ar^+), 543 nm (HeNe), and 633 nm (HeNe). Alternatively, the samples were also illuminated using a supercontinuum laser source (Fianium Supercontinuum SC450, Fianium, Southampton, UK) that was spectrally filtered by an acousto-optic tunable filter (Fianium AOTF V1, Fianium, Southampton, UK), facilitating the use of multi-wavelength laser light. The beam was then spatially filtered, collimated, and directed

through the sample containing the prisms, lenses, and axicons. The light is then collected by the objective. A 25 μm core diameter multimode fiber transmits the collected photons to a fiber-coupled avalanche photodiode (Micro Photon Devices). The multimode collection fiber acts as a 25 μm diameter pinhole in the confocal setup, enabling the collection of light at discrete pixels that build up the intensity scan. Confocal scanning is performed by using a piezo actuated 2-axis stage with nanometric lateral resolution to image in the *x* and *y* directions, and a stepper motor with 50 nm resolution to obtain the optical profile in the *z* direction. The dimension of the optical scan is adjusted such that the scan width exceeds the sample width by 5 μm on either side and the pixels are stepped in increments of 50 nm in the *x* direction and 100 nm in the *z* direction. This oversamples the intensity distribution and resolves the features of the intensity scan projected into the far field. Photons are collected over a 10 ms integration time, and the intensity of the light sources are adjusted with a neutral density filter to constrain the illuminating intensity within the linear range of the photon counting regime.

Waveguide Design and Characterization

The bus waveguide is designed with a 1 μm diameter and the vertical input and output ports have an interport spacing of 250 μm. The total length of the U-shaped bus is 281 μm, containing a central horizontal section measuring 213 μm in length, and two vertically oriented quarter circle arcs with a radius of 18.5 μm (arc length of 29 μm) terminated with a vertical 5 μm section that couples with the characterization setup's fiber array. A 60 μm diameter ring resonator with a core diameter of 1 μm is fabricated with the edge of the ring positioned in the middle of the bus' horizontal central section; the gap between the bus and the ring is spaced laterally by 400 nm, 600 nm, and 800 nm to determine critical coupling.

A near-IR tunable laser source (Photonetics Tunics Purity) driving an erbium-doped fiber amplifer (EDFA) is used to characterize loss in the waveguides. An eight-channel optical fiber array (OZ Optics) was used to couple light into and out of the waveguides. The array has 8 polarization maintaining optical fibers integrated in a patch cord arranged along a line with interspacing of 250 μm. The array facet is polished at 0º to enable coupling at normal incidence. Channel 1 is used to couple light into the input port of U-shaped waveguide and channel 2 is used to measure the output. A manual 3-paddle polarization controller and inline fiber polarizer were used to align the polarization to the slow axis of the input fiber and thereby excite the transverse electric (TE) mode of the microring (i.e., in-plane polarization). The transverse magnetic (TM) mode of the microring (i.e., polarization primarily aligned to the pores) was separately excited using a slow axis to fast axis adapter. The fiber array is mounted on a 1-axis goniometer to enable fine in-plane rotational alignment; the sample is placed on rotational stage on top of an XYZ translational stage to enable coarse rotational and fine translational alignment. Side-view and tilted top-view microscopes are used to aid in alignment. As the laser wavelength is tuned, the light signals transmitted through the device as well as two split off fractions that pass through either a wavelength reference fiber or a plain fiber are converted to photocurrents using fiber coupled photodiodes, amplified with logarithmic amplifiers, and measured on an oscilloscope. The reference consists of a fiber-coupled acetylene gas cell with well-known absorption lines as well as several fiber Bragg gratings (FBGs). This enables the time to wavelength conversion of the oscilloscope data. The plain fiber provides a channel to measure the input power and determine the absolute transmission loss in dB. This overall setup is used to obtain the ring resonator's transmitted intensity spectrum across the telecom C-band.

Multiphoton Imaging

Multiphoton imaging experiments were performed using a Zeiss LSM 710 NLO inverted microscope. A pulsed femtosecond Ti:Sapphire laser (Mai Tai eHP with DeepSee; Newport Corporation, Irvine, CA) with a laser excitation tunable between 690 to 1040 nm with a regular photomultiplier tube or a 32 channel quasar spectral detector was used to characterize the fluorescence emission for objects polymerized using SCRIBE. *Z*-stack acquisitions were performed with a 63x 1.4 NA oil immersion objective with the laser excitation wavelength tuned to 780 nm, giving a lateral resolution on the *x*/*y*-axis of 265 nm and on the *z*-axis of 630 nm[41]. The average scanning laser power was set at 4%. The Zeiss software's "Auto *Z*-Correction" option in the *Z*-stack module was used during image capture to compensate for the loss of excitation light due to absorption and scattering in larger samples. An automated *xy*-stage and stepper motor actuated *z*-stage was used to image *z*-stacks of the SCRIBE written structures at 0.25 μm step size along the *z*-axis and a 0.1 μm pixel size in *xy*. Fields were averaged two times to increase signal to noise ratio. The samples were directly immersed in Immersol index matched oil (n = 1.518) during imaging. Image processing and 3D reconstruction were performed using ImageJ and Amira Software version 6.7.0.

Data availability

The data that support the findings of this study are available from the corresponding author upon reasonable request.

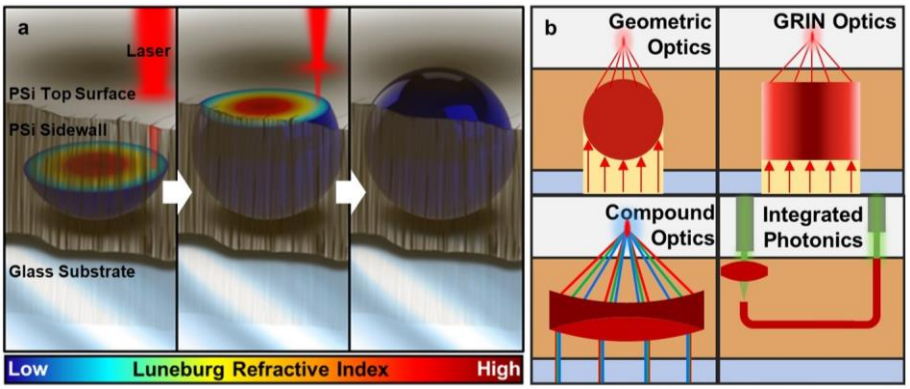

Fig. 1: Overview of devices printed using SCRIBE. a Concept art showing the time-lapse formation of a spherical Luneburg lens printed inside PSi with SCRIBE. **b** Schematic showing four classes of micro-optical elements printed inside a porous scaffold using SCRIBE.

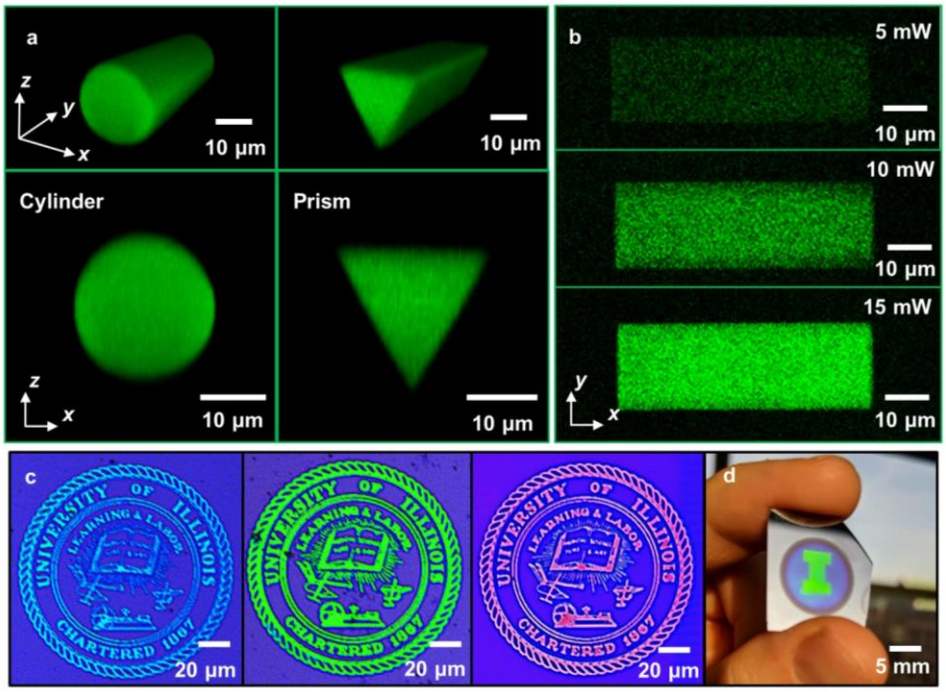

Fig. 2: Freeform geometric and refractive index engineering with SCRIBE. a Multiphoton *xz*-plane and 3D fluorescence scans of a subsurface cylinder and prism. **b** Multiphoton images of three rectangular prisms printed at increasing laser exposures. Objects printed with higher laser exposures fluoresce more intensely. **c** Optical images of three University of Illinois seals printed inside blue PSi DBRs, with increasing printing laser exposure from left to right. A larger redshift in the stopband was observed as the writing exposure was increased. **d** A 5 mm × 7 mm University of Illinois "I" logo printed inside a blue PSi DBR.

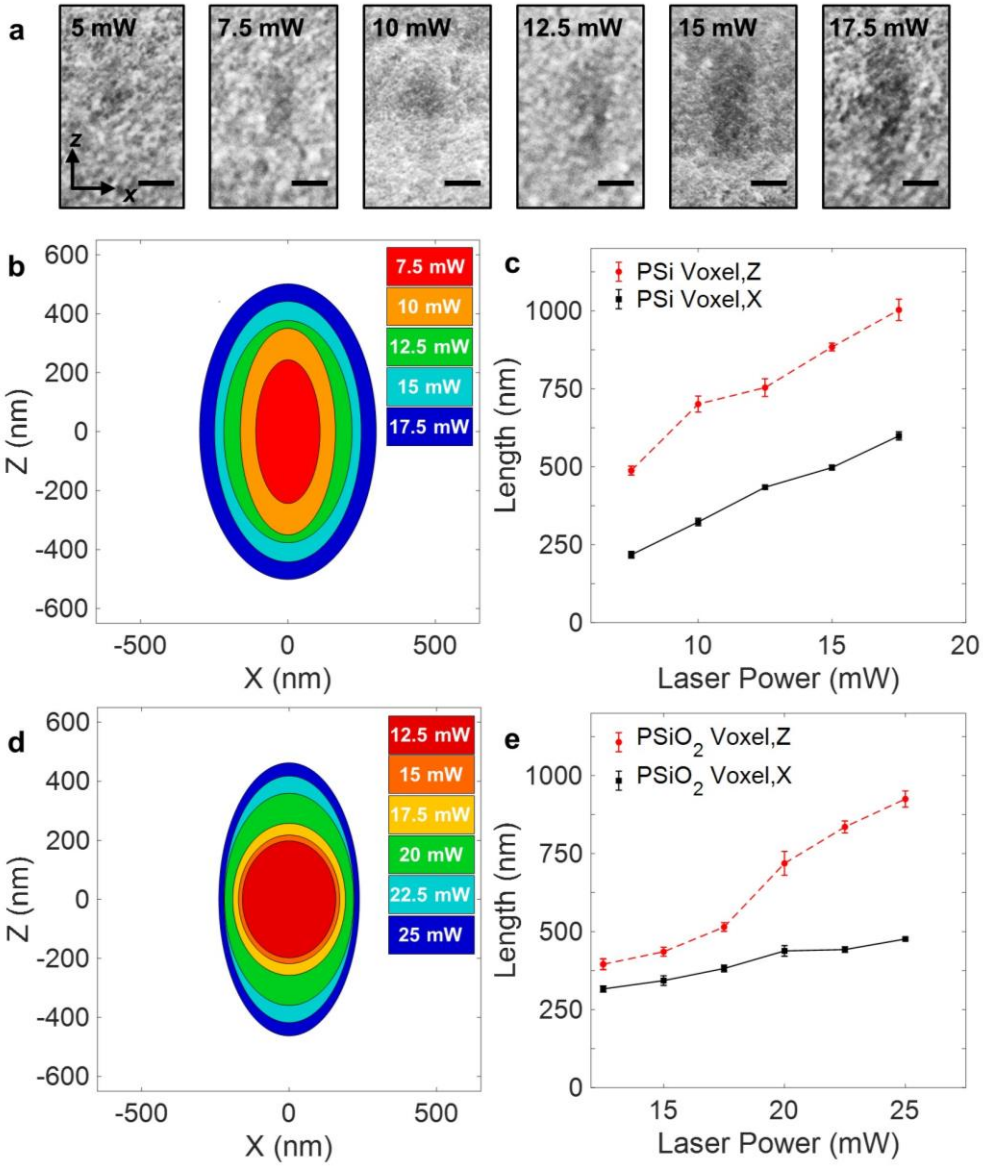

Fig. 3: Subsurface voxel dimensions. a Scanning electron microscopy of fractured cross-sections of line voxels printed inside $PSiO_2$ at different average laser powers. The shape of the voxel becomes more asymmetric and elliptical with increasing laser power, as seen by the contrast between the polymerized region and the porous background. Scale bars are 250 nm. **b, d** Best-fit ellipses for the PSFs in PSi (**b)** and $PSiO_2$ (**d**) in the *xz*-plane for the indicated printing laser powers. **c, e** *x* and *z* dimensions of voxels printed inside PSi (**c**) and $PSiO_2$ (**e**) versus average laser power.

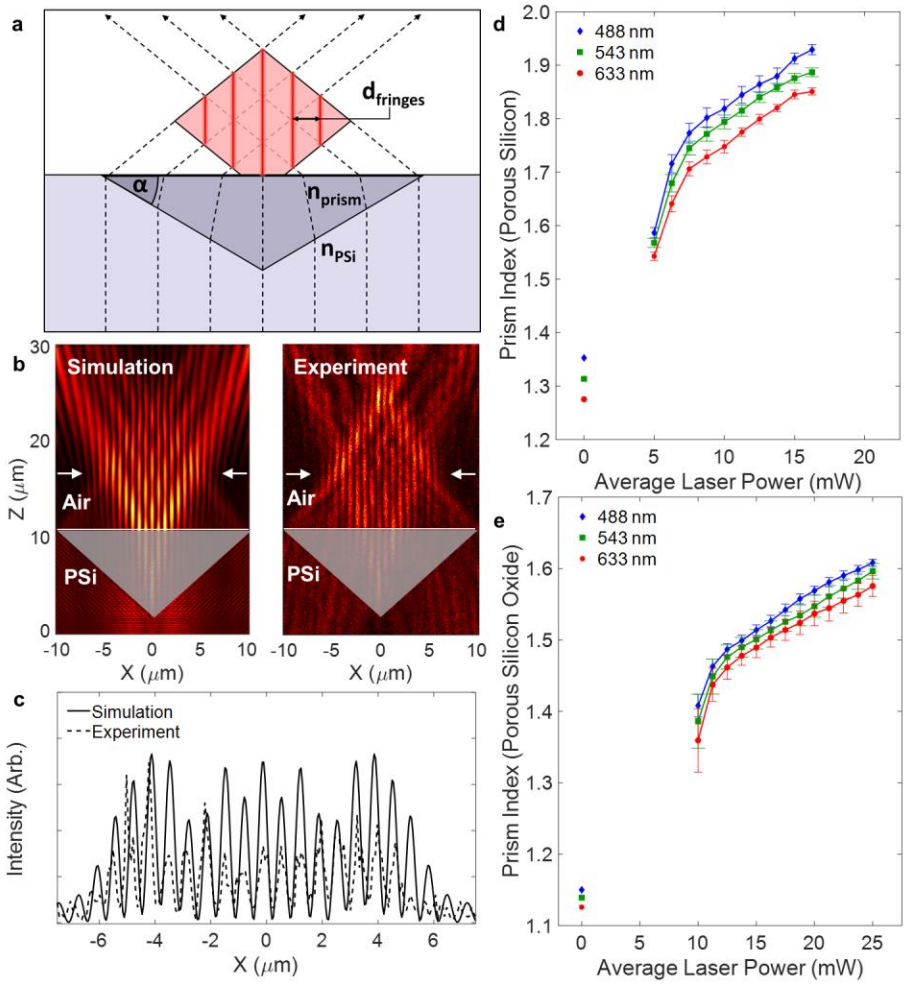

Fig. 4: Characterizing refractive index as a function of writing laser power. a Schematic of an interference pattern produced by a Fresnel biprism. **b** *xz*-plane cross-section of simulated and measured interference patterns at 633 nm produced by a Fresnel biprism with an effective refractive index of 1.82. **c** Overlaid intensity profiles of the simulated and measured interference patterns at the cut line shown in **b**. **d, e** Plots of refractive index versus average laser power of prisms written inside PSi (**d)** and $PSiO_2$ (**e**) for blue (488 nm), green (543 nm), and red (633 nm) light.

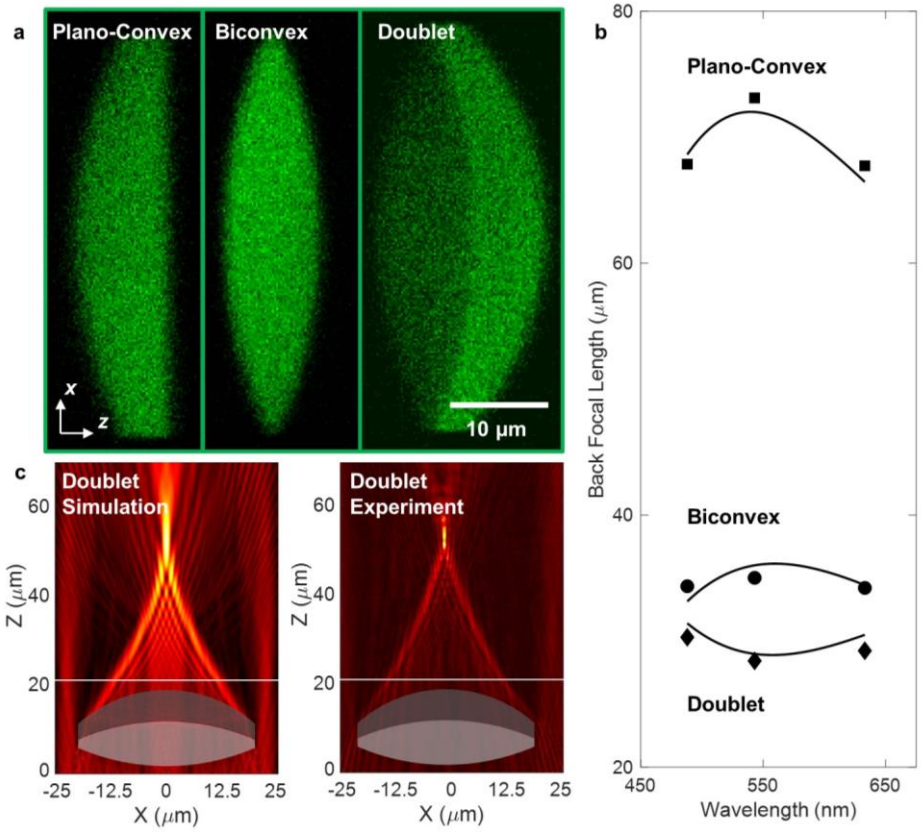

Fig. 5: Dispersion control in geometric optics. a Multiphoton cross-sectional images of microscale plano-convex, biconvex, and achromatic doublet lenses written inside PSi. Each of the doublet's components are rendered using different average laser powers, as indicated by the different fluorescence intensities. **b** Measured focal lengths of the plano-convex (square), biconvex (circle), and doublet (diamond) lenses shown in **a** when illuminated at 488, 543, and 633 nm. Solid traces depict the simulated (Zemax) focal lengths of the elements versus wavelength. **c** Simulated and experimentally measured focal behavior for the doublet shown in **a** at 633 nm.

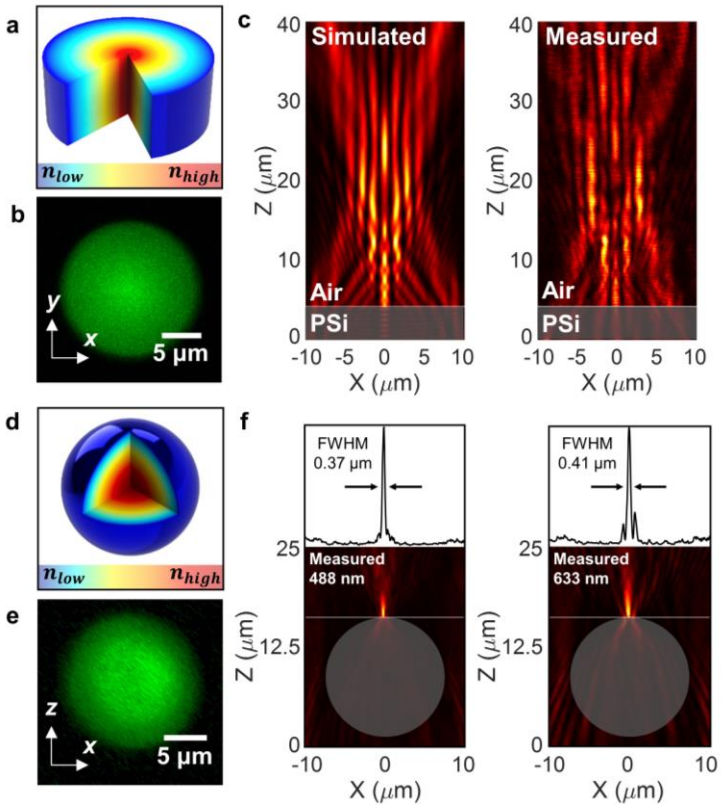

Fig. 6: Gradient refractive index optical elements. a, d 3D cutaway diagrams of a GRIN axicon (**a**) and a spherical Luneburg lens (**d**). **b, e** Measured *xy*-plane multiphoton fluorescence images of a GRIN axicon (**b**) and the spherical midsection of a Luneburg lens (**e)** printed in PSi. **c** Simulated and measured *xz*-plane intensity profiles of interference patterns produced by a GRIN axicon focusing 633 nm light. **f** Measured *xz*-plane intensity profile of a Luneburg lens focusing 488 and 633 nm light to its surface, with a FWHM of 0.37 and 0.41, respectively.

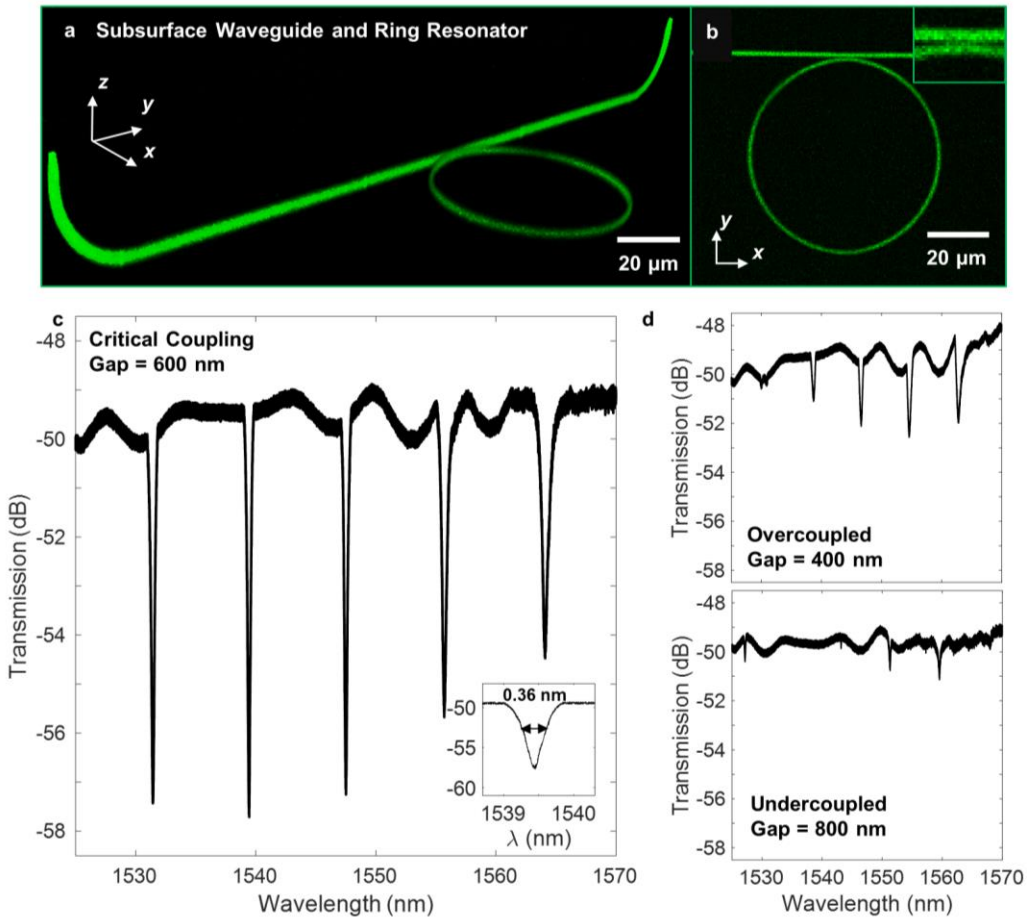

Fig. 7: 3D waveguides coupled to ring resonators. a 3D multiphoton imaging of a subsurface U-shaped waveguide coupled to a microring resonator, with coupling ports displaced by 250 µm. **b** Top view multiphoton image of a 60 µm diameter all-pass microring resonator coupled to a bus waveguide. Inset shows the submicron gap between the microring and the bus waveguide. **c** Experimentally measured microring resonator spectrum for a 600 nm gap device operating in the TE mode (Inset: Resonance near 1539.5 nm shows a 0.36 nm FWHM). **d** Microring spectrum for a 400 nm and 800 nm gap device operating in the TE mode.

References:

1. Hohmann, J. K., Renner, M., Waller, E. H. & Freymann, G. von. Three-Dimensional μ-Printing: An Enabling Technology. *Adv. Opt. Mater.* **3,** 1488–1507 (2015).
2. Gissibl, T., Thiele, S., Herkommer, A. & Giessen, H. Two-photon direct laser writing of ultracompact multi-lens objectives. *Nat. Photonics* **10,** 554–560 (2016).
3. Dietrich, P.-I., Blaicher, M., Reuter, I., Billah, M., Hoose, T., Hofmann, A., Caer, C., Dangel, R., Offrein, B., Troppenz, U., Moehrle, M., Freude, W. & Koos, C. In situ 3D nanoprinting of free-form coupling elements for hybrid photonic integration. *Nat. Photonics* **12,** 241–247 (2018).
4. Deubel, M., von Freymann, G., Wegener, M., Pereira, S., Busch, K. & Soukoulis, C. M. Direct laser writing of three-dimensional photonic-crystal templates for telecommunications. *Nat. Mater.* **3,** 444–447 (2004).
5. Gansel, J. K., Thiel, M., Rill, M. S., Decker, M., Bade, K., Saile, V., Freymann, G. von, Linden, S. & Wegener, M. Gold Helix Photonic Metamaterial as Broadband Circular Polarizer. *Science* **325,** 1513–1515 (2009).
6. Fischer, J. & Wegener, M. Three-dimensional optical laser lithography beyond the diffraction limit. *Laser Photonics Rev.* **7,** 22–44 (2013).
7. Gissibl, T., Thiele, S., Herkommer, A. & Giessen, H. Sub-micrometre accurate free-form optics by three-dimensional printing on single-mode fibres. *Nat. Commun.* **7,** 11763 (2016).
8. Thiele, S., Arzenbacher, K., Gissibl, T., Giessen, H. & Herkommer, A. M. 3D-printed eagle eye: Compound microlens system for foveated imaging. *Sci. Adv.* **3,** e1602655 (2017).
9. Toulouse, A., Thiele, S., Giessen, H. & Herkommer, A. M. Alignment-free integration of apertures and nontransparent hulls into 3D-printed micro-optics. *Opt. Lett.* **43,** 5283–5286 (2018).
10. Yan, W., Cumming, B. P. & Gu, M. High-throughput fabrication of micrometer-sized compound parabolic mirror arrays by using parallel laser direct-write processing. *J. Opt.* **17,** 075803 (2015).
11. Jandura, D., Pudis, D. & Berezina, S. Photonic devices prepared by embossing in PDMS. *Prog. Appl. Surf. Interface Thin Film Sci. Sol. Renew. Energy News IV* **395,** 145–149 (2017).

12. Ergin, T., Stenger, N., Brenner, P., Pendry, J. B. & Wegener, M. Three-Dimensional Invisibility Cloak at Optical Wavelengths. *Science* **328,** 337–339 (2010).
13. Liberale, C., Cojoc, G., Candeloro, P., Das, G., Gentile, F., Angelis, F. D. & Fabrizio, E. D. Micro-Optics Fabrication on Top of Optical Fibers Using Two-Photon Lithography. *IEEE Photonics Technol. Lett.* **22,** 474–476 (2010).
14. Gissibl, T., Schmid, M. & Giessen, H. Spatial beam intensity shaping using phase masks on single-mode optical fibers fabricated by femtosecond direct laser writing. *Optica* **3,** 448–451 (2016).
15. Selimis, A., Mironov, V. & Farsari, M. Direct laser writing: Principles and materials for scaffold 3D printing. *Microelectron. Eng.* **132,** 83–89 (2015).
16. Malinauskas, M., Farsari, M., Piskarskas, A. & Juodkazis, S. Ultrafast laser nanostructuring of photopolymers: A decade of advances. *Phys. Rep.* **533,** 1–31 (2013).
17. Dottermusch, S., Busko, D., Langenhorst, M., Paetzold, U. W. & Richards, B. S. Exposure-dependent refractive index of Nanoscribe IP-Dip photoresist layers. *Opt. Lett.* **44,** 29–32 (2019).
18. Žukauskas, A., Matulaitienė, I., Paipulas, D., Niaura, G., Malinauskas, M. & Gadonas, R. Tuning the refractive index in 3D direct laser writing lithography: towards GRIN microoptics. *Laser Photonics Rev.* **9,** 706–712 (2015).
19. Accardo, A., Blatché, M.-C., Courson, R., Loubinoux, I., Thibault, C., Malaquin, L. & Vieu, C. Multiphoton Direct Laser Writing and 3D Imaging of Polymeric Freestanding Architectures for Cell Colonization. *Small* **13,** 1700621 (2017).
20. Berger, M. G., Arens-Fischer, R., Thönissen, M., Krüger, M., Billat, S., Lüth, H., Hilbrich, S., Theiß, W. & Grosse, P. Dielectric filters made of PS: advanced performance by oxidation and new layer structures. *Thin Solid Films* **297,** 237–240 (1997).
21. Ocier, C. R., Krueger, N. A., Zhou, W. & Braun, P. V. Tunable Visibly Transparent Optics Derived from Porous Silicon. *ACS Photonics* **4,** 909–914 (2017).
22. Waller, E. H., Renner, M. & Freymann, G. von. Active aberration- and point-spread-function control in direct laser writing. *Opt. Express* **20,** 24949–24956 (2012).

23. Guney, M. G. & Fedder, G. K. Estimation of line dimensions in 3D direct laser writing lithography. *J. Micromechanics Microengineering* **26,** 105011 (2016).
24. Chaussard, F., Rigneault, H. & Finot, C. Two-wave interferences space-time duality: Young slits, Fresnel biprism and Billet bilens. *Opt. Commun.* **397,** 31–38 (2017).
25. Doblas, A., Saavedra, G., Martinez-Corral, M., Barreiro, J. C., Sanchez-Ortiga, E. & Llavador, A. Axial resonance of periodic patterns by using a Fresnel biprism. *JOSA A* **30,** 140–148 (2013).
26. Jacques, V., Wu, E., Toury, T., Treussart, F., Aspect, A., Grangier, P. & Roch, J.-F. Single-photon wavefront-splitting interference: An illustration of the light quantum in action. *Eur. Phys. J. D* **35,** 561–565 (2005).
27. Gurram, S. & Nath, A. K. Analysis of tuning of Bragg wavelength of photowritten fiber Bragg gratings during the inscription process using a biprism. *Appl. Opt.* **46,** 2197–2204 (2007).
28. Rizvi, N. H. & Gower, M. C. Production of submicrometer period Bragg gratings in optical fibers using wavefront division with a biprism and an excimer laser source. *Appl. Phys. Lett.* **67,** 739–741 (1995).
29. Zhang, Q., Brown, D. A., Reinhart, L. & Morse, T. F. Simple prism-based scheme for fabricating Bragg gratings in optical fibers. *Opt. Lett.* **19,** 2030–2032 (1994).
30. Ocier, C. R., Richards, C. A., Bacon-Brown, D. A., Krueger, N. A., Clawson, M. K., Soares, J. A. N. T. & Braun, P. V. Optically anisotropic porous silicon microlenses with tunable refractive indexes and birefringence profiles. *Opt. Mater. Express* **10,** 868–883 (2020).
31. Ruffieux, P., Scharf, T., Herzig, H. P., Völkel, R. & Weible, K. J. On the chromatic aberration of microlenses. *Opt. Express* **14,** 4687 (2006).
32. Murray, T. A. & Levene, M. J. Singlet gradient index lens for deep in vivo multiphoton microscopy. *J. Biomed. Opt.* **17,** 021106 (2012).
33. Moore, D. T. Gradient-index optics: a review. *Appl. Opt.* **19,** 1035–1038 (1980).
34. Luneburg, R. K. *Mathematical Theory of Optics*. (Brown University Press, 1944).

35. Zhao, Y.-Y., Zhang, Y.-L., Zheng, M.-L., Dong, X.-Z., Duan, X.-M. & Zhao, Z.-S. Three-dimensional Luneburg lens at optical frequencies. *Laser Photonics Rev.* **10,** 665–672 (2016).
36. Bahadori, M., Yang, Y., Goddard, L. L. & Gong, S. High performance fully etched isotropic microring resonators in thin-film lithium niobate on insulator platform. *Opt. Express* **27,** 22025–22039 (2019).
37. Arbabi, A., Kang, Y. M., Lu, C.-Y., Chow, E. & Goddard, L. L. Realization of a narrowband single wavelength microring mirror. *Appl. Phys. Lett.* **99,** 091105 (2011).
38. Prevedel, R., Yoon, Y.-G., Hoffmann, M., Pak, N., Wetzstein, G., Kato, S., Schrödel, T., Raskar, R., Zimmer, M., Boyden, E. S. & Vaziri, A. Simultaneous whole-animal 3D imaging of neuronal activity using light-field microscopy. *Nat. Methods* **11,** 727–730 (2014).
39. Chambonneau, M., Li, Q., Chanal, M., Sanner, N. & Grojo, D. Writing waveguides inside monolithic crystalline silicon with nanosecond laser pulses. *Opt. Lett.* **41,** 4875 (2016).
40. Davis, K. M., Miura, K., Sugimoto, N. & Hirao, K. Writing waveguides in glass with a femtosecond laser. *Opt. Lett.* **21,** 1729 (1996).
41. Zipfel, W. R., Williams, R. M. & Webb, W. W. Nonlinear magic: multiphoton microscopy in the biosciences. *Nat. Biotechnol.* **21,** 1369–1377 (2003).

Acknowledgments:

This work was sponsored in part by the 'Photonics at Thermodynamic Limits' Energy Frontier Research Center funded by the U.S. Department of Energy, Office of Science, Office of Basic Energy Sciences under Award Number DE-SC0019140 (Brongersma and Braun group focal characterization collaboration), the University of Illinois at Urbana-Champaign College of Engineering Strategic Research Initiative (proof-of-concept studies), and the National Science Foundation (ECCS-1935289) (Goddard group, and Braun group laser patterning).

Affiliations:

Department of Materials Science and Engineering, Materials Research Laboratory, and Beckman Institute, University of Illinois at Urbana-Champaign, Urbana, Illinois 61801, United States
Christian R. Ocier, Corey A. Richards, Daniel A. Bacon-Brown, Tanner J. Garcia, Andrew Rhode, Andrea N. Perry, Dajie Xie, Haibo Gao, Paul V. Braun

Department of Electrical and Computer Engineering, University of Illinois at Urbana-Champaign, Urbana, Illinois 61801, USA
Qing Ding, Raman Kumar, Alexander J. Littlefield, Jinlong Zhu, Lynford Goddard

Department of Mechanical Science Engineering, University of Illinois at Urbana-Champaign, Urbana, Illinois 61801, USA
Kimani C. Toussaint, Paul V. Braun

Carl R. Woese Institute for Genomic Biology, University of Illinois at Urbana-Champaign, Urbana, Illinois 61801, USA
Austin J. Cyphersmith

Geballe Laboratory for Advanced Materials, Stanford University, 476 Lomita Mall, Stanford, CA 94305, USA
Jorik Van de Groep, Jung-Hwan Song, Mark L. Brongersma

Author Contributions Statement:

C. Ocier, C. Richards, D. Bacon-Brown, and P. Braun conceived and developed the subsurface lithographic method used in this work. C. Ocier and C. Richards fabricated the samples. C.

Ocier, C. Richards, D. Bacon-Brown, J. Van de Groep, J. Song, A. Cyphersmith, and M. Brongersma developed the focal characterization methods for this study and measured the optical constants of the subsurface optics. C. Ocier, C. Richards, and A. Cyphersmith imaged the subsurface optics under multiphoton microscopy. C. Ocier, C. Richards, D. Bacon-Brown, T. Garcia, A. Rhode, and Q. Ding designed and characterized the geometric and gradient index lenses. A. Littlefield and C. Ocier designed, simulated, and characterized the photonic nanojet generator devices. R. Kumar, J. Zhu, and L.L. Goddard developed the integrated photonics characterization platform. C. Ocier, C. Richards, T. Garcia, A. Rhode, R. Kumar, and L.L. Goddard designed, fabricated, and characterized the waveguides. C. Ocier and C. Richards carried out the electromagnetic simulations for the geometric and GRIN optics. C. Richards, D. Xie, and H. Gao confirmed the refractive index measurements using electromagnetic simulations. A. Rhode and A. Perry assisted in the design, preparation, and characterization of samples. L. L. Goddard, K. C. Toussaint, Jr., M. L. Brongersma, and P. V. Braun provided critical feedback to improve the design, fabrication process, measurements, and data analysis.

Competing Interests:

L. L. Goddard, K. C. Toussaint, P. V. Braun, J. Zhu, D. Bacon-Brown, C. H. Ocier, Q. Ding, and C. A. Richards claim a U.S. patent on the processes and devices presented in this work through the University of Illinois at Urbana-Champaign.